**Preferred citation:** P.J. Mangin, M.-C Béland and L.M. Cormier. A structural approach to paper surface compressibility – relationship with printing characteristics. In **Products of Papermaking**, *Trans. of the Xth Fund. Res. Symp. Oxford, 1993*, (C.F. Baker, ed.), pp 1397–1427, FRC, Manchester, 2018. DOI: 10.15376/frc.1993.3.1397.

# A STRUCTURAL APPROACH TO PAPER SURFACE COMPRESSIBILITY - RELATIONSHIP WITH PRINTING CHARACTERISTICS

P.J. Mangin, M.-C. Béland, and L.M. Cormier
PAPRICAN
570 St. John's Blvd
Pointe Claire, Que, Canada
H9R 3J9

## ABSTRACT

Three-dimensional topographical maps of paper surfaces under load have been quantified using the confocal laser scanning microscopy. Distributions of the paper surface pores of the same area under different loads were evaluated by the Equivalent Surface Pore (ESP). The ESP roughness of the un-compressed and compressed surfaces of TMP and bleached kraft papers, calendered to the same Print-Surf roughness with different calendering processes, were used to evaluate the local static compressibility of these paper surfaces. Assuming an exponential decay of roughness with pressure, the local static compressibility is defined as the slope of the roughness as a function of the logarithm of the applied pressure. Upon calendering, the local compressibility of the paper surface decreases. The compressibility after calendering depends both on the calendering process and on the furnish. The stiffer TMP fibres present more residual compressibility than the kraft fibres, already pre-collapsed in the uncalendered sheet. The surface compressibility increases with the internal pore volume. The calendered papers were gravure printed at different printing pressures and the number of missing dots counted. A theory is developed which links roughness to ink

coverage. It is proposed that roughness is linearly related to the logarithm of the number of missing dots where the slope represents the surface compressibility. Theoretical derivations have been experimentally verified. It was also found that the static roughness is linearly related to the dynamic roughness.

## INTRODUCTION

The paper surface plays an important role in ink transfer to paper (1-6) and therefore affects the final quality of the printed image. Consequently, numerous methods have been developed to measure surface roughness. However, papers with the same roughness, as evaluated by traditional methods, may lead to very different printing characteristics (6-10). According to many authors, a better relationship would be found if paper surface compressibility were to be taken into consideration (6,8,9,11-14). The evaluation of the printing roughness under compression in a printing nip (6,15) was a first step towards a more comprehensive approach to establishing the relationship between the paper surface properties and the paper printing characteristics. In this approach, the paper surface was described by a model pore whose roughness is equivalent to the average roughness of the paper and whose shape corresponds to the shape of an average surface pore.

This paper proposes both an extension and a practical application of the model-pore approach. Confocal microscopy is used to evaluate the roughness of the same paper area under increasing pressure. A novel compression apparatus that was used is also briefly described. From the analysis of the variations of the roughness as a function of the applied pressure, a local static compressibility parameter is derived. An equation is also proposed which relates the roughness under load, the local static compressibility, and the number of missing dots in gravure.

## APPROACH

In order to establish a relationship between the paper surface compressibility and its printing characteristics, a three-step approach was devised. First, a method was developed to acquire three-dimensional (3D) topographical maps of the same paper area under different pressures. Second, the compression of the paper surface was described by the deformation of the model pore at different pressures. The local static compressibility was thus calculated. Third, the paper samples were gravure printed to test for a correlation between the number of missing dots, the paper roughness under load, and the static local compressibility.

## EXPERIMENTAL

### Confocal Principle.

Discrimination in the Z-direction is the main advantage of confocal microscopy over conventional microscopy. The confocal principle is shown in **Figure 1**. At the laser source, a first pinhole is used to obtain point source illumination. This pinhole is fixed in size. The light going through the objective and reflected off the object is directed to the detector by a beam splitter. A variable pinhole is placed in front of the detector and thus only information corresponding to the focal spot light on the object reaches the detector. A point-by-point image is obtained by scanning the beam over an XY plane. The XY sectioning therefore depends on the opening of the detector pinhole: the more open the pinhole, the more the XY sectioning property deteriorates, i.e. the focal plane is thicker in appearance. When the pinhole is fully opened, the images resemble those obtained with a conventional microscope.

Images of single focal planes are therefore acquired and sectioning of the object is possible by moving the location of the focal plane within the Z-direction of the object. This results in a stack of images originating from different depths within the object. A detailed 3D topographical map of the surface of the object is reconstructed from the focal plane images. This way of establishing a map of the surface is particularly interesting for paper surfaces since it is non-disturbing. The 3D topographical map ranges from the top of the highest fibre in the field of view to the bottom of the deepest open pore. In addition, proper marking of the sample location on the microscope stage allows for the same paper surface area to be imaged.

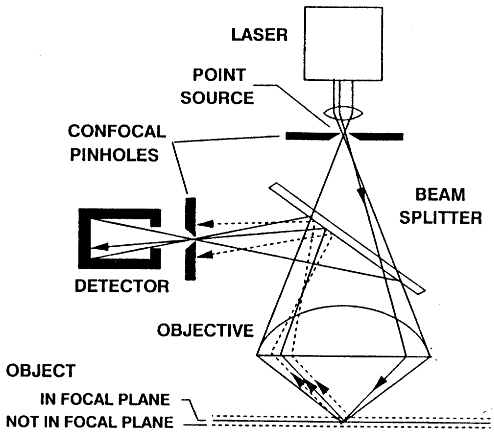


Fig. 1 Confocal Microscopy Principle.

## Compression Apparatus.

The compression apparatus presented in **Figure 2a** was designed in order to evaluate paper surfaces under load. The apparatus respects weight, strength, and imaging constraints imposed by the confocal microscope. The use of a special aluminum alloy allows the weight of the compression apparatus to remain lower than the weight that would affect the accuracy in depth of the micro-moving stage. The apparatus is also sufficiently robust to allow high pressures to be attained without deformation of the compressing surfaces. The top disk of the compression apparatus is constructed from tool steel, yielding a pressure range of about 0-5 MPa to be applied without deformation. This pressure range corresponds to that of the main printing processes. Finally, the top of the compression disk is machined to match the profile of the objective. A 2 mm diameter hole, made in its centre, allows the objective to focus on the paper surface under load. During testing, the sample is placed in the centre of the bottom part then covered with a circular coverslip

(**Figure 2b**). The steel compression disk is then positioned on top of the coverslip (**Figure 2c**). Once the load is applied to the disk, the coverslip compresses the paper. Needle bearings, placed on top of the steel disk, prevent torque transfer when pressure is applied with a torque wrench.

Fig. 2a

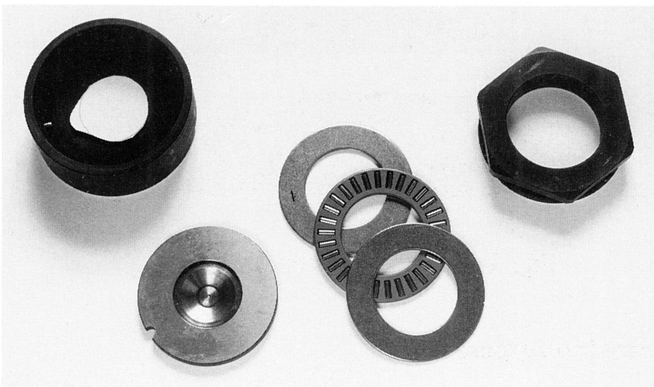

**Pressure Calibration**

The pressure applied at a given torque value was measured separately for each paper sample, using Fuji presscale film. During mounting, the paper sample was separated from the pressure sensitive film by a coverslip of the same diameter as that used on the top of the sample. Each load was tested independently. The pressure sensitive film was removed and the optical density was

Fig. 2b

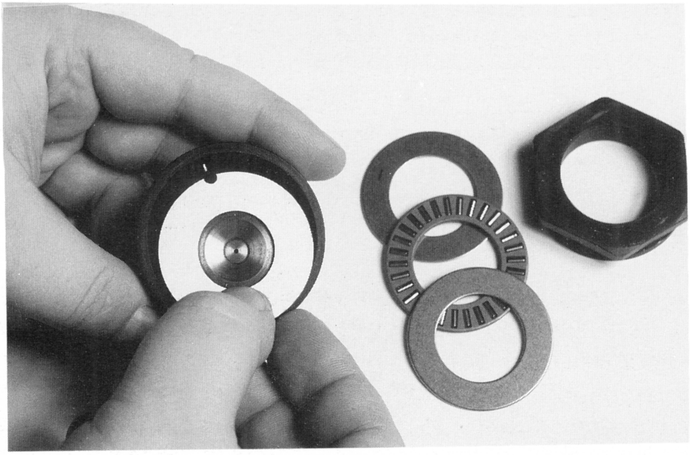

Fig. 2c

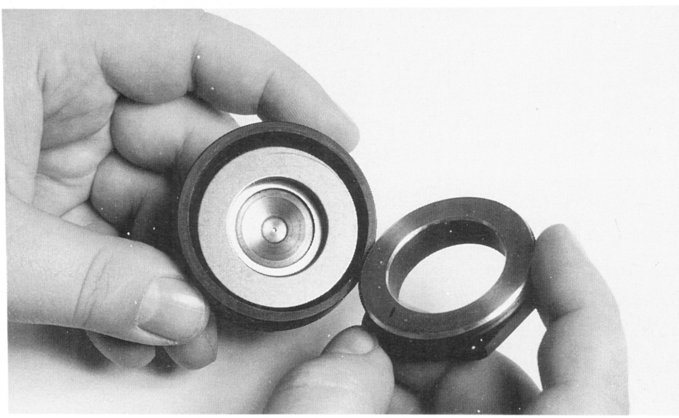

Fig. 2 Compression apparatus: (a) main components; (b) sample mounted inside the apparatus; and (c) apparatus prepared for pressure application.

measured with a Macbeth densitometer TR927 that has a measuring spot of 2.5 mm in diameter. Using the calibration scale provided with the film, optical density measurements were converted to applied pressure. The pressure was evaluated from the average of 5 optical density readings centered on the area compressed by the coverslip. As the pressure calibration procedure is destructive, a different paper area was imaged to evaluate the paper surface and compressibility properties.

**Samples.**

Two commercial uncalendered samples, one newsprint made from 100% TMP and one 100% bleached kraft paper, were calendered using conventional, soft nip, and temperature gradient calendering to a target PPS (S10) roughness of 3.7 $\mu$m. The calendering conditions are detailed in **Table 1**. The non-calendered samples were also evaluated, for a total of 8 samples. Physical properties of the samples are listed in **Table 2**.

| Sample | Nips | Load | Temperature °C | Roll speed m/min |
|---|---|---|---|---|
| TMP-CC | 3 | 60-60-60 kN/m | 50 | 300 |
| TMP-SN* | 2 (1 soft) | 3 psi | - | - |
| TMP-TG | 1 | 40 kN/m | 204-202 | 300 |
| K-CC | 3 | 60-60-60 kN/m | 50 | 300 |
| K-SN* | 2 (1 soft) | 6 psi | - | - |
| K-TG | 1 | 35 kN/m | 200-200 | 300 |
| CC | conventional calendering | | | |
| SN | soft nip calendering | | | |
| TG | temperature gradient | | | |
| * | performed at Abitibi-Price | | | |

**Table 1.** Calendering Conditions

| Sample | Caliper µm | PPS-S10 µm | PPS-S20 µm | Internal Pore Volume mL/g |
|---|---|---|---|---|
| TMP-NC | 125 | 7.80 | 5.80 | 1.304 |
| TMP-CC | 78 | 3.66 | 2.37 | 0.991 |
| TMP-SN | 96 | 4.39 | 2.75 | 1.098 |
| TMP-TG | 83 | 3.78 | 2.34 | 1.005 |
| K-NC | 107 | 6.99 | 5.01 | 0.652 |
| K-CC | 83 | 3.36 | 2.69 | 0.509 |
| K-SN | 88 | 3.56 | 2.84 | 0.520 |
| K-TG | 88 | 3.40 | 2.69 | 0.595 |

TMP basis weight is 45.7 g/m$^2$ and K basis weight is 69.9 g/m$^2$

**Table 2.** Physical Properties

**Printing.**

The calendered samples were gravure printed with an IGT printability tester at four pressures, namely 2.03, 3.08, 4.13 and 4.91 MPa. The Heliotest NC gravure cylinder used contained areas with gravure cell diameters of 85 µm and 110 µm. The number of missing dots corresponding to each printing pressure are given in **Table 3**.

**Imaging.**

A Leica confocal laser scanning microscope was used to acquire reflection mode images of the paper surfaces. The field size was 313 µm by 313 µm, as obtained with a 16X (air) objective. A set of 16 confocal images were acquired for each topographical map. The total depth of acquisition was optimized for each image independently, since uncompressed surfaces require a larger Z-range than do those under load. In order to calculate a local compressibility parameter, exactly the same area was imaged after each pressure increase. One area on the undisturbed sample was selected and imaged, and the same area was imaged at each pressure.

**Repeatability.**

Repeatability of CLSM image acquisition has been assessed by Svoboda (16) and has been measured on our instrument as 2.8% (17). The CLSM static compressibility measurements were repeated on three samples. When results were analyzed for covariance to take into account the effect of initial uncompressed roughness on compressibility, the repeatability was found to be 15.6%.

| Sample | Missing Dots 2.03 MPa | Missing Dots 3.08 MPa | Missing Dots 4.13 MPa | Missing Dots 4.91 MPa |
|---|---|---|---|---|
| TMP-NC | --- | --- | --- | --- |
| TMP-CC | 45 | 4 | 1 | 0 |
| TMP-SN | 157 | 13 | 2 | 0 |
| TMP-TG | 423 | 33 | 3 | 1 |
| K-NC | --- | --- | --- | --- |
| K-CC | 631 | 91 | 36 | 13 |
| K-SN | 873 | 190 | 62 | 28 |
| K-TG | 1497 | 244 | 57 | 20 |

**Table 3.** Gravure Printing: Heliotest Missing Dots (110 $\mu$m)

## QUANTIFICATION OF 3D TOPOGRAPHICAL MAPS

Each 3D topographical map yields a histogram of the pixel frequency distribution as a function of the grey level in the image. The histograms obtained for each image are transformed into area versus depth distribution curves according to equations 1 and 2,

$$D_i = \Delta Z - \frac{\Delta Z}{256} * i \tag{1}$$

$$A_i = \frac{S}{f} * F_i \tag{2}$$

where $D_i$ is the depth at a grey level i, $\Delta Z$ is the total Z-range of the acquisition, $A_i$ is the total area of pixels corresponding to grey level i, S is the field of view, f is the total number of pixels of the image, and $F_i$ is the frequency value corresponding to the grey level i. The surface reference plane, at depth z = 0, has been arbitrarily set at an intensity level that represents 0.01% or more of the total surface. These curves represent the distribution of the surface pores as a function of depth. The data are further transformed into normalized cumulative area versus depth. The cumulative distribution curves represent the profile of the paper surface pores as a function of depth. It is therefore possible to generate an Equivalent Surface Pore (ESP) by a $\pi/2$ rotation of the cumulative distribution curve (6,15). The ESP is a model pore whose shape represents the profile of an average pore of the paper surface. Its volume corresponds to the roughness of the uncompressed paper. A roughness value is therefore derived from the general topographical equation,

$$G_n = \left[ \frac{1}{A} \int_0^A z^n \, da \right]^{1/n} \tag{3}$$

where $G_n$ is the $n^{th}$ order roughness, A is the measured area, and da is an element of surface area corresponding to a depth z.

For most paper applications, like the PPS air-leak roughness (18) or the model-pore approach (6,15), the calculated roughness corresponds to the 3rd order roughness. Accordingly, the ESP roughness becomes:

$$G_3 = \left[ \frac{1}{A} \int_0^A z^3 \, da \right]^{1/3} \tag{4}$$

The ESP roughness calculated from the model-pore approach was first presented by Mangin (15). The application of this approach to CLSM images and data sets was described in detail by Mangin and Béland (17). For each 3D topographical map, the ESP roughness is directly calculated from equation 5,

$$G_3 = \left[ \sum_{0}^{256} D_i^3 * (Ac_{i+1} - Ac_i) \right]^{1/3} \tag{5}$$

where $Ac_i$ is the normalized cumulative area at intensity i.

## RESULTS AND DISCUSSION

### Paper Surfaces Under Load.

Generating 3D topographical maps of the same paper surface, either uncompressed or under load, is an unique capability resulting from the combined use of the novel compression apparatus with confocal microscopy. This capability is illustrated in **Figure 3** where the same area of the uncalendered bleached kraft sample is shown uncompressed **(3a)** and under load **(3b and 3c)**. All 3D topographical maps are grey-coded for height, where deeper areas are darker. The increasing area of the paper surface occupied by lighter greys as load is applied indicates how the compression of the surface proceeds. The smaller pores appear almost unaffected, remaining relatively constant in all the images, as exemplified by the

Fig. 3(a)


Fig. 3(b)

Fig. 3(c)

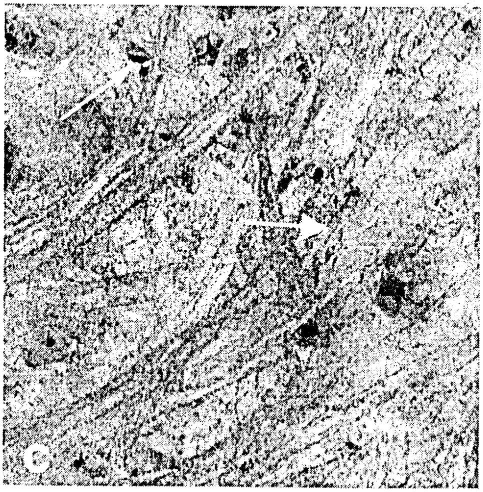


Fig. 4(a)

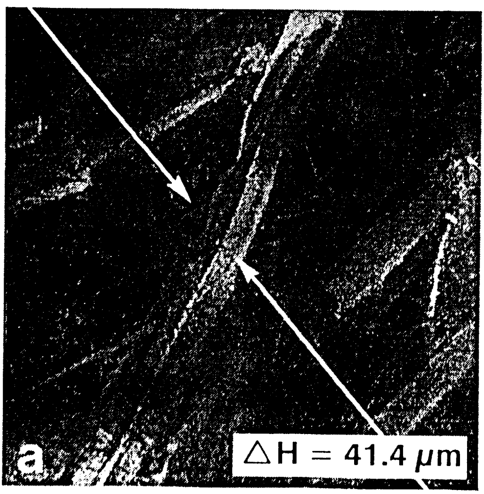

Fig. 4(b)

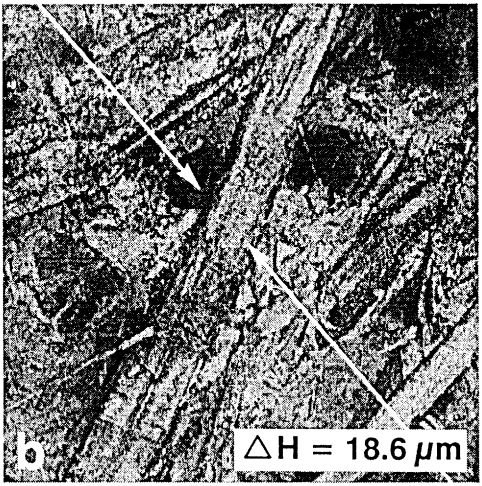


Fig. 4(c)

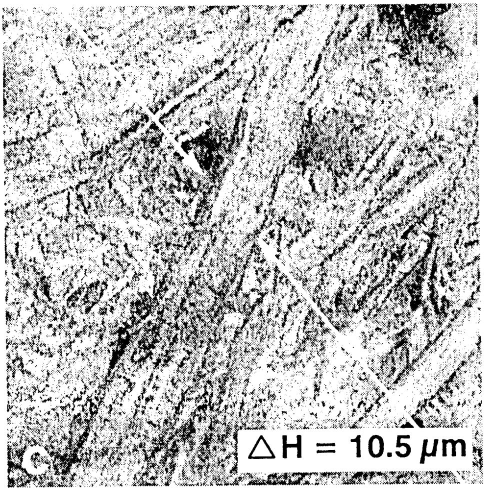


Fig. 4 Registered 3D topographical maps of the same area of an uncalendered 100% TMP newsprint. On all the images, a height difference $\Delta H$, has been measured between identical features as indicated by the arrow pairs. (a) uncompressed, $\Delta H = 41.4\ \mu m$; compressed at (b) 1.65 MPa, $\Delta H = 18.6\ \mu m$; and (c) 5.24 MPa, $\Delta H = 10.5\ \mu m$.

pore indicated by the small arrow. Small pores are subtended by close-neighbouring fibres which bear the main portion of the load. Accordingly, they do not conform during compression and tend to remain open. By contrast, the larger pores tend to close upon compression, as exemplified by the pore indicated by the large arrow. Large pores are subtended by fibres further apart which do not support the load as effectively. Accordingly, large pores tend to close upon compression. The behavioral difference between small and large pores under compression has considerable implications for printing. Among others, it suggests that surface pore size and shape distributions, and how they change upon compression, will substantially affect print quality. Finally, 3D topographical maps show the detailed structure of entire surface pores. As such, they provide a representative sampling of the paper surface, both uncompressed and under load, and should serve as a reference to evaluate the limitations of the more indirect roughness evaluation methods.

In addition to the qualitative interpretation, a first level quantitative evaluation of the images is performed by measuring the height difference between two structural features as load is applied. For example, **Figure 4** shows the same area of the uncalendered TMP sample uncompressed **(4a)** and under load **(4b and 4c)**. The height difference between the upper portion of the central fibre that can be seen and one of the pores to the left of this fibre, indicated by the two arrows, is 41.4 $\mu$m in the uncompressed state. When load is applied, even at a low level (0.009 MPa), the height difference between these same two features decreases to 38.4 $\mu$m. The height difference at the highest pressure applied (**Figure 4c**, 5.24 MPa) is only 10.5 $\mu$m. The height difference variation as a function of pressure is shown in **Figure 5**. As expected from previous work (6,8,9,15), the height difference decreases exponentially.

A more complete analysis of how the paper deforms under load may be performed on the entire 3D topographical maps. The area versus depth distributions representing the distribution of the surface pores as a function of depth corresponding to the images in **Figure 4** are shown in **Figure 6a** while the cumulative distribution curves are shown in **Figure 6b**.

Fig. 5 Height difference variations measured between arrow pairs, as obtained from the images in Figure 4, as a function of applied pressure.

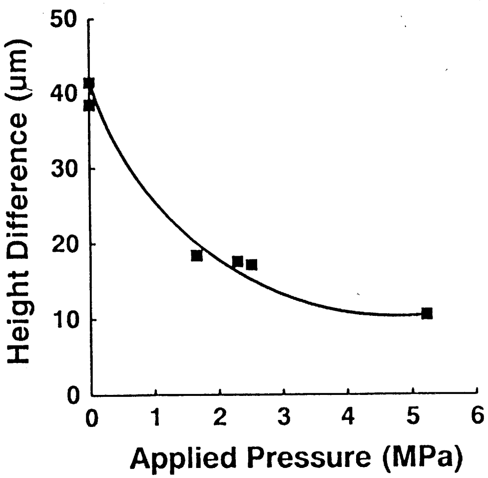


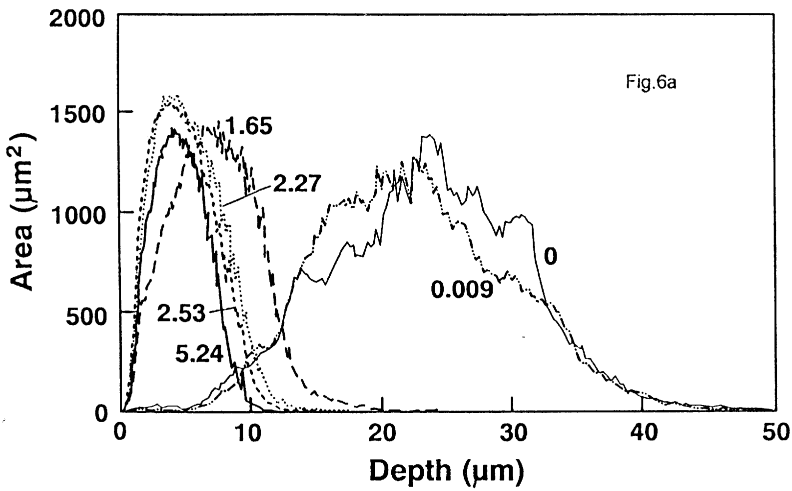


Fig. 6 (a) Surface pore distribution curves for the TMP-NC sample as a function of depth for the different applied pressures; (b) corresponding normalized cumulative curves; (c) corresponding ESPs.

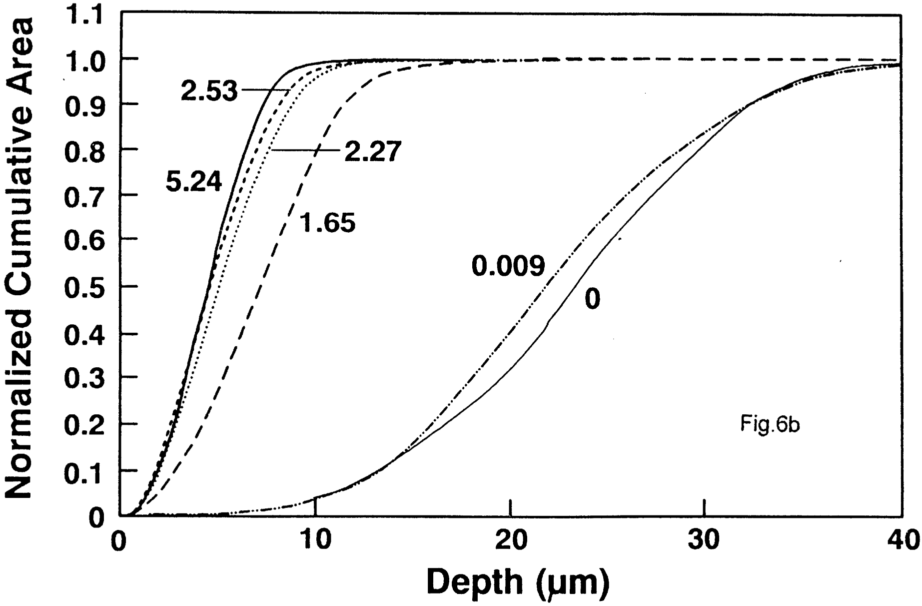
Normalized Cumulative Area
1.1
1.0
0.9
0.8
0.7
0.6
0.5
0.4
0.3
0.2
0.1
0
2.53
2.27
5.24
1.65
0.009
0
0
10
20
30
40
Depth (μm)

Fig.6b

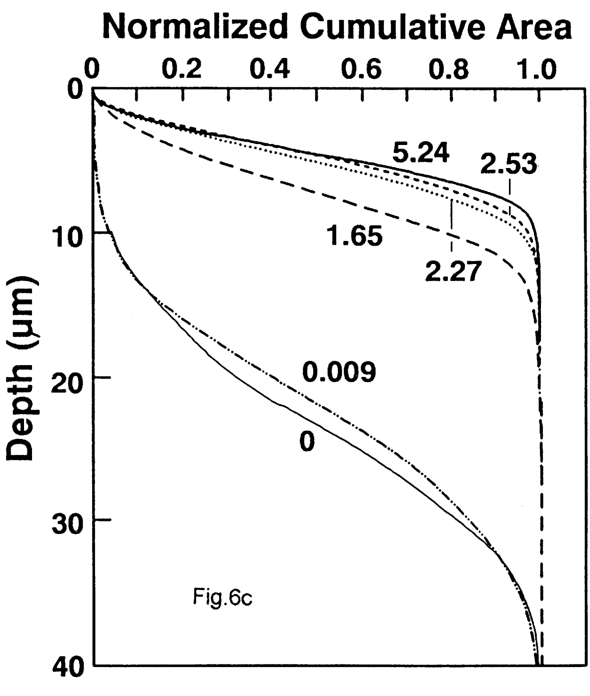
Normalized Cumulative Area
0
0.2
0.4
0.6
0.8
1.0
0
10
20
30
40
Depth (μm)
5.24
2.53
1.65
2.27
0.009
0

Fig.6c

**Figure 6a** provides useful descriptive information about the uncompressed paper surface and how it changes under load. For instance, it shows that the distance between the highest and the lowest elements of a paper surface, either uncompressed (0 MPa) or slightly compressed (0.01 MPa), is about 50 $\mu$m. The range decreases to about 10-15 $\mu$m for loads higher than 1 MPa. In addition, it also shows that the pore distribution for a given area on the paper is shifted towards the surface as load is applied. The fact that structural elements are closer to the surface as compression proceeds is also reflected in **Figure 6b**. In this figure, the surface reference is the y axis that corresponds to a depth of 0. When pressure increases, the cumulative distributions shift towards the y axis, indicating that structural elements have moved closer to the surface.

**Evaluation of the Local Static Compressibility.**

In **Figure 6c**, the cumulative distributions have been rotated by $\pi/2$ to represent the ESPs. From each curve, the ESP roughness is calculated according to equation 5. The roughness values thus calculated for each sample are listed in **Table 4**. As expected, the roughness decreases with applied pressure. The variation in roughness as a function of the applied pressure is shown in **Figure 7a** for the ESPs of **Figure 6c**. It was previously found that the PPS roughness (8,9), the ESP roughness calculated from 3D profilometric maps obtained with a stylus profilometer (15), and the printing roughness derived from ink transfer analysis (6) all decay exponentially with pressure. Accordingly, we assume that the same relationship holds true for the ESP roughness calculated from 3D topographical maps. As seen in **Figure 7b**, the roughness varies linearly as a function of the pressure logarithm. It is therefore possible to calculate a compressibility parameter that is independent of the applied pressure. Such a compressibility parameter, calculated from equation 6, provides an intrinsic characteristic of the paper surface.

$$G_3 = G_3(1) + K_s' \log(P) \tag{6}$$

where $G_3$ is the ESP roughness, $G_3(1)$ is the ESP roughness at a pressure P of 1 MPa (log P = 0), and $K'_s$ is the local static compressibility.

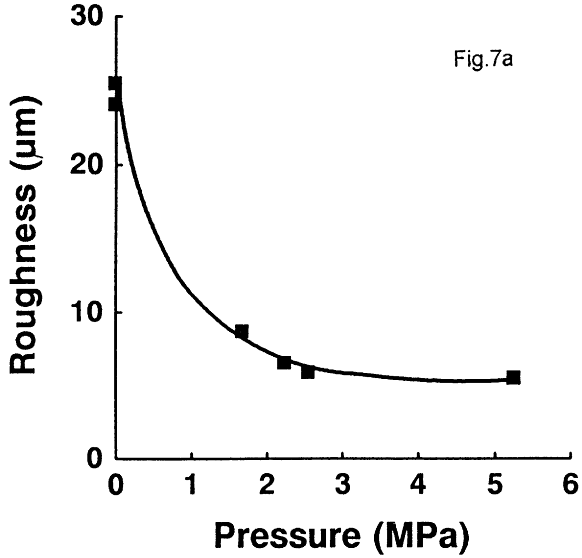


Fig. 7 ESP roughness for the TMP-NC sample: (a) as a function of applied pressure; and (b) as a function of the pressure logarithm.

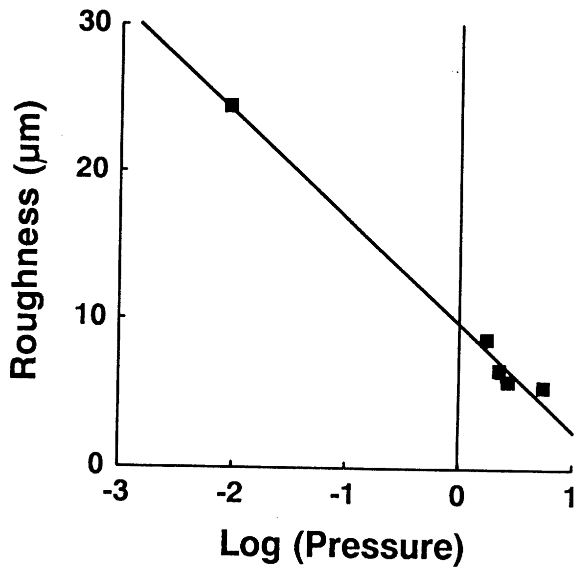


Fig.7b

In **Figure 7b**, representing the TMP-NC sample, the compressibility is 7.15 $\mu$m. The compressibility values of the eight samples and their corresponding coefficient of determination (average $r^2$ = 0.968) are given in **Table 5**. The compressibility after calendering depends both on the calendering process and on the furnish. The stiffer TMP fibres present more residual compressibility than the kraft fibres, already pre-collapsed in the uncalendered sheet.

**Correlation with Print Quality.**

In gravure printing, ink coverage is measured in terms of printed dot area and therefore excludes the unprinted area between the half-tone dots. If the number of dots printed corresponds to the number of cells on the gravure cylinder, the ink coverage is 100 percent. A print quality parameter arises from counting missing dots on a test print. The coverage, Cov, is then given by equation 7,

$$Cov = \frac{(N_T - N)\ a_d}{N_T a_o} \tag{7}$$

where $N_T$ is the total number of dots on the gravure cylinder, N is the number of missing dots counted, $a_o$ is the dot area on gravure cylinder, and $a_d$ is the average printed dot area. In the Heliotest NC, partially transferred dots are not considered as "missing".

| | | | | | | | |
|---|---|---|---|---|---|---|---|
| TMP-NC | P, MPa | 0 | 0.01 | 1.65 | 2.25 | 2.55 | 5.25 |
| | $G_3$, $\mu$m | 25.3 | 24.4 | 8.70 | 6.50 | 5.95 | 5.45 |
| TMP-CC | P, MPa | 0 | 0.01 | 1.65 | 1.95 | 2.25 | 4.10 |
| | $G_3$, $\mu$m | 13.1 | 10.5 | 3.85 | 3.30 | 3.45 | 3.50 |
| TMP-SN | P, MPa | 0 | 0.01 | 1.65 | 2.00 | 2.80 | 5.15 |
| | $G_3$, $\mu$m | 13.3 | 12.8 | 5.05 | 4.75 | 4.60 | 4.35 |
| TMP-TG | P, MPa | 0 | 0.01 | 1.70 | 1.95 | 2.55 | 4.40 |
| | $G_3$, $\mu$m | 15.4 | 15.1 | 5.75 | 4.95 | 4.70 | 4.85 |
| K-NC | P, MPa | 0 | 0.01 | 1.65 | 1.80 | 2.15 | 5.60 |
| | $G_3$, $\mu$m | 12.0 | 9.25 | 4.80 | 4.55 | 4.55 | 4.35 |
| K-CC | P, MPa | 0 | 0.01 | 1.60 | 1.70 | 2.60 | 3.60 |
| | $G_3$, $\mu$m | 7.80 | 5.90 | 3.60 | 3.90 | 3.80 | 3.95 |
| K-SN | P, MPa | 0 | 0.01 | 1.70 | 1.80 | 2.05 | 4.30 |
| | $G_3$, $\mu$m | 13.1 | 10.1 | 5.70 | 5.15 | 5.75 | 5.80 |
| K-TG | P, MPa | 0 | 0.01 | 1.60 | 1.80 | 2.10 | 5.75 |
| | $G_3$, $\mu$m | 13.0 | 7.30 | 6.35 | 6.15 | 5.90 | - |

**Table 4.** ESP Roughness Corresponding To Applied Pressure.

| SAMPLE | $K'_S$ | Intercept | $r^2$ * |
|---|---|---|---|
| TMP-NC | 7.15 | 9.70 | 0.991 |
| TMP-CC | 2.85 | 4.58 | 0.982 |
| TMP-SN | 3.22 | 6.06 | 0.989 |
| TMP-TG | 4.06 | 6.69 | 0.987 |
| K-NC | 1.88 | 5.32 | 0.981 |
| K-CC | 0.85 | 4.13 | 0.936 |
| K-SN | 1.81 | 6.29 | 0.942 |
| K-TG | 0.52 | 6.26 | 0.932 |

* calculated from ESP roughness under compression, i.e. 5 data points

**Table 5.** Local Static Compressibility

Equation 7 implies that the coverage is a function of both the number of missing dots and the average printed dot area. In practice however, only the number of missing dots is considered. The decrease in average printed dot area due to an increased paper roughness is usually neglected, and $a_d$ is considered to be approximately equal to $a_0$. Consequently, ink coverage becomes a function of the number of missing dots, such as

$$Cov = 1 - \frac{N}{N_T} \tag{8}$$

It is well accepted (2,19) that ink coverage functions usually take the form of asymptotic exponential functions such as

$$Cov = 1 - e^{-kX} \tag{9}$$

where k is a coverage or smoothness parameter and X is the ink weight on the printing plate (2,19). As ink weight on the printing plate increases, ink coverage increases and the unprinted pore volume decreases. In parallel, when printing pressure is increased, ink coverage increases and the surface pore volume decreases (6). Consequently, we propose that ink coverage as a function of pressure will also follow an asymptotic exponential relationship. This is expressed in equation 10,

$$Cov = 1 - e^{-kP} \tag{10}$$

where P is the printing pressure, and k is a conformability parameter.

When P = 0, there is no ink transfer, and the coverage is 0. When the printing pressure P is high, $e^{-kP}$ approaches 0, and the coverage is close to 1, where all dots are uniformly transferred to the paper surface. The increase in coverage is related to the fact that the paper surface conforms more and more to the gravure printing cylinder as the printing pressure is increased. Accordingly, the parameter k describes the conformability of the paper surface with increasing printing pressure.

From equations 8 and 10, equations 11 and 12 can be derived.

$$\frac{N}{N_T} = e^{-kP} \tag{11}$$

and

$$\log N = \log N_T - \frac{1}{2.3} kP \tag{12}$$

Equation 12 predicts that the logarithm of the number of missing dots is linearly related to the printing pressure. Furthermore, it also predicts that the value of the intercept will be log $N_T$. For the

Heliotest NC, $N_T$ = 15620, and the value for the intercept predicted by our model is 4.19.

Experimental results are given in **Table 6**. As predicted by equation 12, the mean value for the intercept is 4.11 with a standard deviation of 0.27. This is well within experimental error, and confirms that partially transferred dots may be neglected. These experimental results also verify both the linear relationship between the logarithm of the number of missing dots and the printing pressure, and the relationship proposed in equation 10, between coverage and printing pressure.

Previous work (6) on the evaluation of the dynamic compressibility of the paper surface in a printing nip has shown that

$$R_g = R_g(1) + K'_D \log P \tag{13}$$

where $R_g$ is the printing roughness, or roughness measured dynamically in the printing nip, $R_g(1)$ is the printing roughness for a pressure value of 1 MPa, and $K'_D$ is the dynamic compressibility. The equation is similar to the one proposed by Bristow for the evaluation of static compressibility with the Parker Print-Surf (8).

From equations 12 and 13, it follows that the number of missing dots is related to both the roughness of the paper in the printing nip and to the dynamic paper compressibility, as given by equation 14:

$$R_g = R_g(1) + K'_D \log \left[ -\frac{2.3}{k} \log \frac{N}{N_T} \right] \tag{14}$$

*REGRESSION DATA FOR*

$$\log N - \log N_T - \frac{1}{2.3} kP$$

| SAMPLE | Slope, - 1/2.3 k | Conformability, k $MPa^{-1}$ | log $N_T$ | $r^2$ |
|---|---|---|---|---|
| TMP-CC | 0.798 | 1.83 | 3.92 | 0.975 |
| TMP-SN | 0.915 | 2.10 | 4.01 | 0.993 |
| TMP-TG | 0.936 | 2.15 | 4.45 | 0.990 |
| K-CC | 0.571 | 1.31 | 3.87 | 0.976 |
| K-SN | 0.520 | 1.20 | 3.94 | 0.992 |
| K-TG | 0.654 | 1.50 | 4.46 | 0.996 |

log $N_T$ intercept, theoretically predicted value is 4.19
log N logarithm of the number of missing dots

**Table 6.** Relationship Between Log(Number of Missing Dots) and the Printing Pressure.

The roughness of paper in the printing nip is difficult to measure. However, using printing and PPS roughness data from Mangin and Geoffroy (6), we find that the dynamic roughness, $R_g$, is linearly related to the static roughness, $G_3$, measured at the same nominal pressure, with an average coefficient of determination of 0.944. This is expressed as

$$R_g = a + bG_3 \tag{15}$$

where a is the intercept and b is the slope of the linear relationship.

Accordingly, equations 14 and 15 give

$$G_3 = \left(\frac{R_g(1) - a}{b}\right) + \frac{1}{b}K'_D \log\left[-\frac{2.3}{k}\log\frac{N}{N_T}\right] \qquad (16)$$

which relates the static roughness $G_3$ to the dynamic compressibility and the number of missing dots in gravure.

In the absence of dynamic roughness measurements, equation 16 provides a way to test the relationship in equation 14 by using the static roughness values calculated from the 3D topographical maps. This was verified experimentally with a coefficient of determination $r^2$ of 0.94.

Finally, a comparison of compressibility, either static (**Table 5**) or dynamic (from **Equation 16**), and conformability (**Table 6**) reveals that the TMP samples are both more compressible and more conformable than the kraft samples. It should be emphasized that the conformability parameter is included in equation 14 relating compressibility, roughness, and gravure missing dots. However, an independent evaluation of the surface conformability is outside the scope of this work.

**Effect of Paper Structure on Compressibility.**

Considering that the internal pore volume reflects the global porous structure of the paper, a relationship between internal volume and compressibility is expected. As can be seen in **Figure 8**, compressibility increases with the internal pore volume, as measured with Hg intrusion porosimetry. This supports the finding that pore size distribution will affect the final print quality, since paper samples having the same PPS roughness but different total pore volumes show different compressibility values. From **Figure 8**, we propose the following symbolic relationship between the static compressibility, $K_S'$, and the internal pore volume, V:

$$K_S' \propto V^2 \tag{17}$$

The quadratic relationship between internal pore volume and the measured compressibility was verified with an $r^2 = 0.904$.

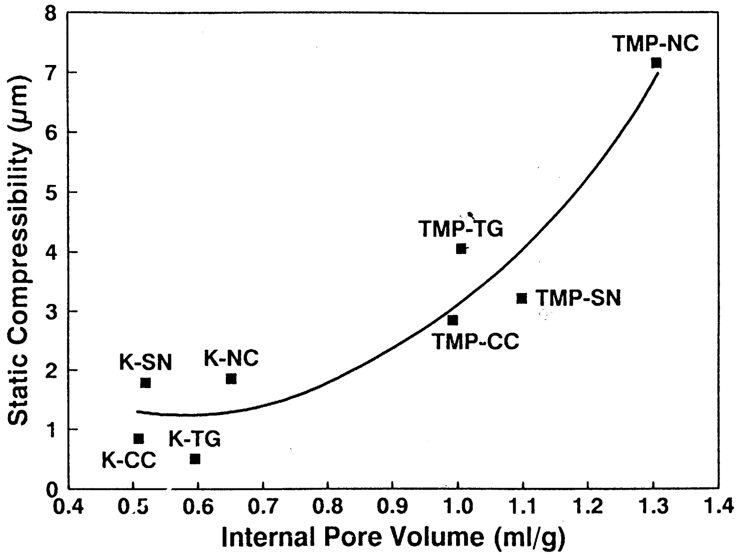


Fig. 8 Local static compressibility as a function of the internal pore volume.

## CONCLUSIONS

Three-dimensional topographical maps of <u>the same paper area</u> imaged prior to and during compression have been obtained by the combined use of a novel compression apparatus and confocal microscopy.

Three-dimensional topographical maps provide a representative sampling of the paper surface structure, both un-compressed and under load, and should serve as a reference to evaluate the limitations of the more indirect roughness tests.

A local static compressibility parameter has been calculated from the variations of the ESP roughness of the same paper area under increasing pressure. This compressibility was found to be proportional to the square of the internal pore volume.

Relationships have been derived that relate either the printing roughness or the static roughness to the number of missing dots on a gravure test print and to the surface compressibility. The theoretical derivations have been verified experimentally.

## ACKNOWLEDGEMENTS

In keeping with the team spirit that flourished throughout the course of this work, the authors would like to recognize the support of the many co-workers whose prompt responses to our requests were much appreciated. In particular, the authors thank J. Hamel, B. Kreklewetz and S. Regev for useful discussions and much appreciated involvement in the planning, construction and modification of the compression apparatus; M. Gratton and S. Smallwood for providing and calendering the samples; J. Chasle for the porosimetry measurements; J. Dalphond, T. Manfred, and S. Sauriol for the Heliotest NC prints and dot counting; and D. Lord for her help in developing the pressure calibration method. Abitibi-Price is also thanked for performing the soft-nip calendering. Dr. B. Jordan is thanked for useful comments in the technical review of the manuscript. K. Duarte is also thanked for his help and patience in providing photographic support services during the scope of this work.

## REFERENCES


1. Pihl, L., The ink transfer to paper, Svensk Papperstidning, Vol. 55, 358-362 (1952).

2. Walker, W.C. and Fetsko, J.M., A concept of ink transfer in printing, TAGA Proc., 139-149, 1955 and American Ink Maker, 33, No. 12, 38 (1955).

3. Hultgren, K., Calculation of ink transfer in letterpress printing, Proc., 11th Intern. Conf. Printing Research Inst., Canandaigua, N.Y., U.S.A., W.H. Banks Ed., 3-32 (1971).

4. Bery, Y., Three-equation ink transfer model, Adv. in Printing Science and Technology, W.H. Banks Ed., Pentech Press, London, Vol. 16, 206-234 (1981).

5. De Grâce, J.H. and Mangin, P.J., A Mechanistic Approach to Ink Transfer. Part I: Effect of Substrate Properties and Press Conditions, Adv. in Printing Science and Technology, W.H. Banks Ed., Pentech Press, London, Vol. 17, 312-332 (1984).

6. Mangin, P.J., and Geoffroy, P., Printing roughness and compressibility, Fundamentals of Papermaking, 9th Fundamental Research Symposium, Cambridge, England, Vol.2, 951-978 (1989), and Adv. in Printing Science and Techn., W.H. Banks Ed., Pentech Press, London, , Vol.20, 249-265 (1990).

7. Mangin, P.J. and De Grâce, J.H., A new method for evaluating the printing characteristics of newsprint, TAPPI/CPPA IPGAC, 135-143 (1984).

8. Bristow, J.A., The surface compressibility of paper - A printability property, Adv. in Printing Science and Techn. W.H. Banks Ed., Pentech Press, London, Vol. 15, 403-420 (1980).

9. Bristow, J.A. and Ekman H., Paper properties affecting gravure print quality, TAPPI 64(10): 115-118 (1981).

10. Heintze, H.U., Press operation and gravure print quality, TAPPI 65(6): 109-112 (1982).

11. Roehr W.W., Effect of smoothness and compressibility on the printing quality of coated paper, TAPPI 38(11): 660-664 (1955).

12. Henry, P.M., Compressibility and resiliency tester, TAPPI 39(1): 137A (1956).

13. Hsu, B., The influence of paper compressibility on ink penetration, Appl. Sci. Res., Section A, Vol 10: 277-285 (1961).

14. Ullman U. and Qvarnström, I., Influence of surface smoothness and compressibility on print unevenness, TAPPI 59(4): 98-101 (1976).

15. Mangin, P.J., The measurement of paper roughness: A 3D profilometry approach, Adv. in Printing Science and Techn., W.H. Banks Ed., Pentech Press, London, , Vol.20, 218-235 (1990).

16. Svoboda, K.K.H. "Comparative Studies of Biorad and Leica Confocal Laser Scanning Microscopes", Proceedings of SCANNING 91, I-91 (1991).

17. Mangin, P.J. and Béland, M.-C., The three-dimensional evaluation of paper surfaces using confocal microscopy. Research and Development Applications, IARIGAI, Munchen, Germany (Sept. 1993).

18. Parker J.R., An air leak instrument to measure printing roughness of paper and board, Paper Technology, 6(2): T32-T36 (1965).

19. Mangin, P.J., Lyne, M.B., Page, D.H. and De Grâce, J.H., Ink Transfer Equations. Parameters Estimation and Interpretation, Adv. in Printing Science and Techn., W.H. Banks Ed., Pentech Press, London, Vol. 16, 180-205 (1982).

## Transcription of Discussion

# A STRUCTURAL APPROACH TO PAPER SURFACE COMPRESSABILITY – RELATIONSHIP WITH PRINTING CHARACTERISTICS

### Prepared Contribution

**P J Mangin**, M.-C. Béland & L M Cormier

**Prof B Lyne, Royal Institute of Technology, Sweden**

I would like to hear this paper in the non data compression mode to have time to study your new compression technique. I think you published papers showing that the Parker Printsurf tends to over estimate the roughness because of the lateral air leaks in the sheet. I noticed in your graphs that you are getting pore depths that are much greater than the Parker Printsurf values with this optical technique (depths around 15-30 microns). Can you explain the difference between the air leak and optical results?

**P Mangin**

Yes, very easily. First the actual target value S10 was 3.5 and we had a 3.7 microns. In which case we do have this kind of lateral flow and only a small difference between the Parker Print-Surf roughness and the confocal roughness. The 15 micrometres value for pore depths is basically for the uncompressed paper. At higher compressions, similar to the Parker Print-Surf, we have found very similar values with about 20-28% difference, no more. This is what we expected to find. It is very consistent with previous work and we even have some work ongoing related to this. So there is no contradiction. However, you are raising a very good point. For instance, when we are measuring the caliper, we have some small compressions. My first reaction at looking at the uncompressed paper roughness was astonishment too. It is a huge value. From top to bottom we have sometimes 50 micrometres and I knew caliper was about 80. Was there something wrong with the data? But compression changes roughness very dramatically in the first portion of the compression curve. That's the explanation.

**B Phillips, Shotton Paper Company plc, UK**

How do the pressures that you have been using in your apparatus relate to (a) gravure printing and (b) Offset printing?

**P Mangin**

They do relate. Pressures used in offset printing are more in the order of about 4 MPa. We have modified the compression system I have shown you by reducing the aperture for the measuring of compression. We also had to modify the bottom part of the system because the high pressure created some buckling. We can reach nowadays up to 8-10 MPa according to the paper samples. Our next step is also to look at the offset printing and to transpose the approach. It will be easy because the coverage in offset can be measured by image analysis. So we will not have to care about missing dots.